Available online at www.sciencedirect.com
SCIENCE DIRECT®
Applied Clay Science 31 (2006) 1 – 15
Applied CLAY Science
www.elsevier.com/locate/clay

Influence of firing conditions on ceramic products: Experimental study on clay rich in organic matter

L. Maritan [a,*], L. Nodari [b], C. Mazzoli [a,c], A. Milano [b], U. Russo [b]

[a] *Dipartimento di Mineralogia e Petrologia, Università di Padova, C.so Garibaldi 37, I-35137 Padova, Italy*
[b] *Dipartimento di Scienze Chimiche, Università di Padova, Via Marzolo 1, I-35131 Padova, Italy*
[c] *Istituto di Geoscienze e Georisorse, CNR, Padova, C.so Garibaldi 37, I-35137 Padova, Italy*

Received 24 May 2004; received in revised form 15 April 2005; accepted 12 August 2005
Available online 6 October 2005

Abstract

The effect on ceramic products of firing conditions in the presence of abundant organic matter is assessed here experimentally by reproducing two ancient firing techniques: *pit firing*, characterised by a high heating rate and short residence time in a reducing atmosphere; *kiln firing*, with a low heating rate and long residence time in an oxidising atmosphere. As expected, *pit firing* conditions produced uniformly reduced ceramics, and gehlenite, diopside and spinel occurred at suitable temperatures (above 900 °C). Interestingly, in *kiln firing* conditions, sandwich structures formed in the ceramics, in which mineral assemblages and Fe oxidation state turned out to be different in the black core with respect to the margin. Spinel, cordierite and metallic Fe formed in the core, whereas hematite and spinel, in addition to gehlenite and diopside, crystallised in the margin at suitable temperatures (above 800 °C). Therefore, despite the oxidising atmosphere of the firing, reducing conditions occurred in the core, suggesting sluggish oxygen diffusion within the pottery. In addition, decomposition of reactant mineral phases and crystallisation of new mineral products in *pit firing* conditions occurred at temperatures about 50 °C higher than in *kiln firing* conditions, indicating that residence time strongly controlled reaction kinetics, as higher temperatures (i.e., a higher degree of reaction overstepping) are required when residence time is lower. On the contrary, illite broke down at a lower temperature than expected in both sets of firing conditions. This is interpreted as the effect of reduced water fugacity caused by burning of the organic matter.

Keywords: Organic matter; Heating rate; Firing atmosphere; Mössbauer spectroscopy (TMS); Diffractometric analysis (XRD); Fourier transformed infrared spectroscopy (FTIR)

1. Introduction

Plasticity is an essential parameter, which determines the attitude of the clayey material moulded and modelled in pottery production, a criterion for clay classification (Marsigli and Dondi, 1997) determined by measuring the Atterberg limits. The presence of organic matter may significantly increase clay plasticity (Husein Malkawi et al., 1999). Organic matter occurs as humus in soils excavated for pottery production (Nannipieri, 1993; Rivero et al., 1998) or may be deliberately added by the potter (Johnson et al., 1988) in order to reach the required rheological features of the raw material. If adequate conditions occur during firing, organic matter may completely burn, contributing toward increasing secondary porosity. But what is the role of organic matter in the firing process and how does it affect the sequence of reactions in the resulting ceramic products?

* Corresponding author. Tel.: +39 049 8272032; fax: +39 049 8272010.
E-mail address: lara.maritan@unipd.it (L. Maritan).

0169-1317/$ - see front matter © 2005 Elsevier B.V. All rights reserved.
doi:10.1016/j.clay.2005.08.007

In the present work, clay rich in organic matter is examined, and variations in mineral assemblages during heating are evaluated by step-heating experiments. In order to reach the firing conditions of archaeological pottery, two different ancient firing techniques are reproduced: i) *pit firing*, a technique in which pots were placed in an open pit, covered by straw and wood, fired and then covered with earth in order to preserve heat and increase the firing temperature; ii) *kiln firing*, a more highly developed technique, for which permanent or partially permanent structures were used, and in which the fire was separated from the pots by the firing chamber.

The varying arrangement and location of pots with respect to the fire result in significantly different firing conditions. *Pit firing* has a high heating rate (tens of degrees per minute), short residence time (maximum temperature maintained constant for a certain period of time) (a few minutes), and reducing conditions, excluding vessels deliberately exposed to the air while still at high temperature (Rye, 1981; Gosselain, 1992). In *kiln firing*, the heating rate is generally low (a few hundreds of degrees per hour), residence time is long (many hours), and redox conditions may vary depending on the type of kiln, although they are generally oxidising (Rye, 1981; Gosselain, 1992).

2. Experimental and analytical procedures

A clayey material (sample AES7a) was collected in the area of Lozzo Atestino, south of Mount Lozzo (Eastern Euganean Hills, Padova, Italy) by hand-drilling alluvial deposits at a depth of 1 m. The content of organic matter was determined by Thermo-Gravimetric (TGA) and Differential Thermal Analyses (DTA) with a custom-built instrument at the Istituto di Geoscienze e Georisorse (IGG), CNR, Padova, by heating the sample up to 1000 °C in an oxidising atmosphere. The Atterberg limits and plasticity index of the starting clayey material were measured according to CNR-UNI 10014 norm (1964), and chemical composition was determined by X-ray fluorescence (XRF) spectroscopy, using a Philips PW 2400 spectrometer, equipped with a Rh tube, at the Dipartimento di Mineralogia e Petrologia (DMP), University of Padova. The sample was prepared as a bead of calcined powder and $Li_2B_4O_7$, using a dilution ratio of 1:10. Geological standards were used for calibration. The FeO/FeO_{tot} ratio was determined by titration with potassium permanganate and Mössbauer spectroscopy.

The clayey material was used without tempering and prepared in 32 discs 5 by 1.5 cm. After drying at room temperature for 7 days and then at 50 °C in an oven for 24 h, the disks were fired at temperatures from 300 to 1100 °C, in successive temperature steps of 50 °C, in both reducing and oxidising conditions, for a total of 32 runs. *Pit firing* conditions were reproduced by firing samples in a CFM Carbolite tube furnace installed at the Department of Geology (University of Glasgow), with a heating rate of 25 °C/min, residence time of 10 min, and cooling rate of 100 °C/h. A reducing atmosphere was obtained by fluxing N_2 at a pressure of 0.5 bars, after filtering with H_2SO_4, $CaCl_2$ and $Mg(ClO_4)_2$ to avoid air contamination. *Kiln firing* conditions were reproduced with an MT furnace at DMP, equipped with a digital microprocessor (Digitronik DCP200, Yamateke-Honeywell) for firing curve control, by firing samples in air [$f(O_2) \sim 0.2$ bars], at a heating rate of 200 °C/h, residence time of 6 h, and cooling rate of 50 °C/h.

Fired samples were also analysed by Mössbauer spectroscopy, using a conventional constant-acceleration spectrometer and a room temperature Rh matrix ^{57}Co source, at the Dipartimento di Scienze Chimiche (DSC), University of Padova. The hyperfine parameters isomer shift (δ), quadrupole splitting (ΔE_Q), full linewidth at half maximum (Γ), expressed in mm/s, and the internal magnetic field (H), expressed in Tesla, were obtained by means of a standard least-squares minimisation technique. The spectra were fitted to Lorentzian line shapes using a minimum number of sextets and doublets. δ is quoted relative to metallic Fe at room temperature (RT). Low temperature (80 K) spectra were also collected in order to detect any superparamagnetic phenomena, which might have been caused by Fe oxide nanoparticles.

Mineral assemblages in both clayey material and fired samples were determined by X-ray diffraction (XRD) analysis on a Philips PW 3710 diffractometer using CuK_α radiation, at IGG.

For samples displaying a sandwich structure, the reddish-brown margins were mechanically separated, when possible, from the black cores by means of a glass chisel in order to avoid Fe contamination, and analysed separately. All specimens were ground in an agate mortar under acetone, to avoid oxidation, and analysed by X-ray diffraction (XRD) and Mössbauer spectroscopy.

Fourier Transform Infrared (FTIR) spectroscopy was also applied to examine all samples, using an FTIR Nicolet spectrometer equipped with a DTGS detector, at DSC. Samples were dispersed in anhydrous KBr (Aldrich, +99%) using a dilution ratio of 1:100, and FTIR spectra were collected in the range 4000–400 cm^{-1}.

Total C was determined on a CE-Instruments EA 1110 automatic elemental analyser (EA) at IGG, equipped with an AS 200 autosampler and Mettler Toledo AT21 comparator, according to the analytical procedure described in Ragazzi et al. (2003). 10 mg of powered sample was placed in a tin capsule and simultaneously analysed for carbon, hydrogen, nitrogen and sulphur based on dynamic flash combustion and GC separation (He gas carrier) followed by thermal conductivity detectors (TCD). Calibration standards were prepared from known amounts of sulphanilamide ($C_6H_8N_2O_2S$).

3. Results and discussion

The chemical composition of the starting clayey material resulted to be: SiO_2 (56.78), TiO_2 (1.02), Al_2O_3

(20.12), Fe_2O_{3tot} (7.58), MnO (0.07), MgO (2.33), CaO (7.70), Na_2O (0.88), K_2O (2.81) and P_2O_5 (0.29), with a loss on ignition of 18.47 wt.%. In addition, FeO = 1.27 wt.% was determined by titration, and consequently Fe_2O_3 was recalculated to 4.95 wt.% from Fe_2O_{3tot}. Mineral composition was determined by XRD, DTA, TGA and FTIR spectroscopy. Illite, quartz, chlorite, plagioclase, calcite and K-feldspar were identified in the XRD spectrum. Some of these mineral phases were also identified from the DTA and TGA patterns (Fig. 1) by comparison with data from the literature (Mackenzie, 1957; Stucki and Bish, 1990). In particular, the DTA diagram (Fig. 1a) shows a peak at 125 °C and an inflexion point at 200 °C, probably due to the removal of hygroscopic water from illite and organic matter. The latter can absorb as much as 4 times its own weight in water, due to the large number of functional hygroscopic groups in these molecules (De Nobili and Maggioni, 1993). Two exothermic peaks in the range 350–450 °C are attributed to the oxidation of organic matter, leading to a weight loss of about 6%, as also shown by the TGA pattern in Fig. 1b. Moreover, the DTA diagram (Fig. 1a) shows decomposition of chlorite at 540 °C and decarbonation of calcite at 840 °C.

The high content of organic matter confers good plasticity on this clayey material, as indicated by the liquid limit, plastic limit, and plasticity index (Husein Malkawi et al., 1999), which turned out to be 75, 37 and 38, respectively.

The FTIR spectra and relative second derivative patterns (Fig. 2) further confirm XRD, DTA and TGA data. In particular, the O–H stretching region (Fig. 2b) displays two characteristic signals of structural hydroxylic groups in chlorite at 3621 and 3696 cm^{-1} (Farmer, 1974), and those of adsorbed water at 3433 and 1635 cm^{-1}. Moreover, the absorption bands at 1430, 873 and 721 cm^{-1} are related to calcite (Fig. 2c), whereas that at 1031 cm^{-1} (Fig. 2d) is due to the Si–O stretching mode (Farmer, 1974; De Benedetto et al., 2002). Additional minor absorption peaks in the Si–O stretching region are magnified in the second derivative pattern (Fig. 2c) and attributed to chlorite and illite (De Benedetto et al., 2002). As regards organic matter, two weak signals at 2921 and 2851 cm^{-1} (Fig. 2b) are probably due to aliphatic C–H stretching bands (Claret et al., 2003), although the relatively small amount of organic matter and high Si–O absorption make the signals difficult to identify. On the basis of XRD and chemical data, as the organic matter represents about 6 wt.% of the

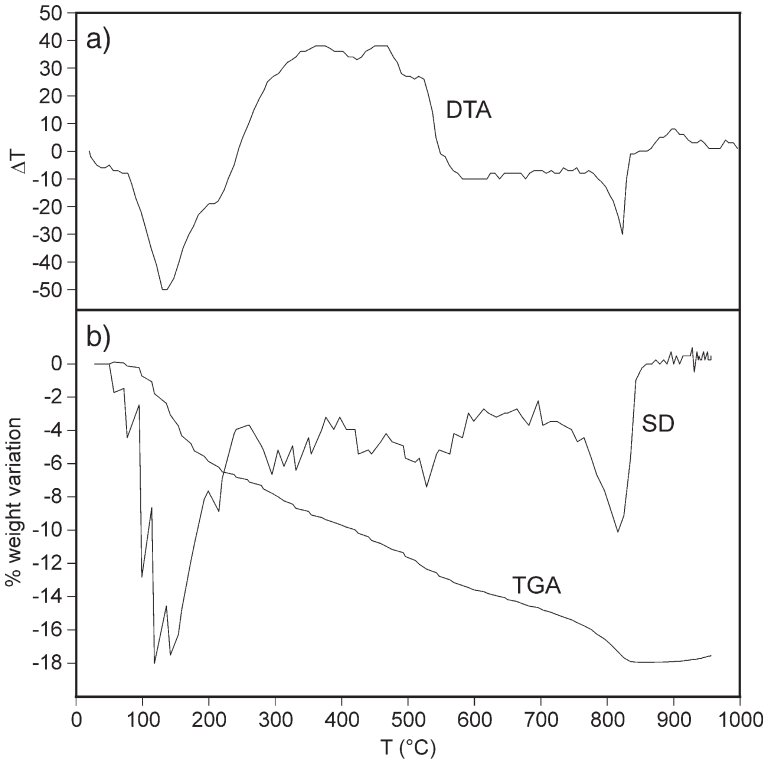

Fig. 1. (a) Differential thermal (DTA) diagram; (b) thermo-gravimetric (TGA) and second derivative (SD) diagram.

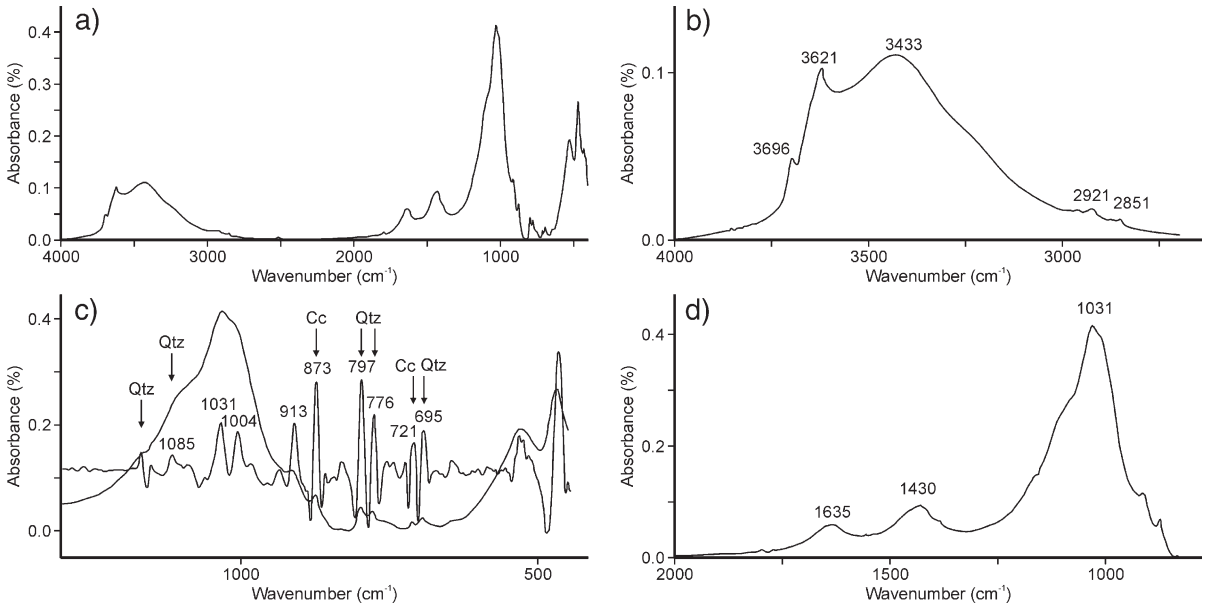

Fig. 2. IR spectrum (a) of starting clayey material, with details on hydroxyl (b), carbonate (c) and silicate (d) regions. Second derivative profile in range 1300–450 cm^{-1} is also reported in (c). Cc: calcite; Qtz: quartz.

air-dried sample, normal composition was determined by FASES software (Krajewski et al., 1985) obtaining the following concentrations in wt.%: illite (28), plagioclase (23), quartz (18), chlorite (13), calcite (5), K-feldspar (3) and others (4).

Mössbauer measurements were performed at RT and 80 K. Two main octahedral sites due to Fe(III) were identified, the first (site A) characterised by a high ΔE_Q (0.68 mm/s), a δ value of 0.35 mm/s, and a Γ value of 0.34 mm/s; the second (site B) had a low ΔE_Q (0.51

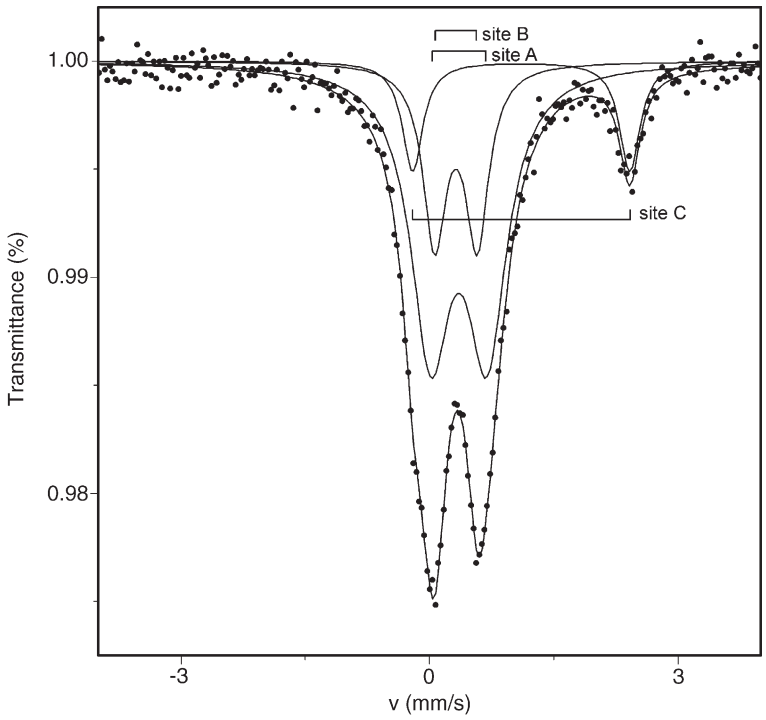

Fig. 3. Room temperature Mössbauer spectrum of starting clayey material.

Table 1
Room temperature Mössbauer parameters for samples prepared in *kiln firing* conditions

T (°C)	Margins						Cores					
	δ (mm/s)	ΔE_Q or $2\varepsilon_Q$ (mm/s)	Γ (mm/s)	H (T)	A (%)	Attrib.	δ (mm/s)	ΔE_Q or $2\varepsilon_Q$ (mm/s)	Γ (mm/s)	H (T)	A (%)	Attrib.
Clay	0.35	0.68	0.58		63	Fe(III) A	0.35	0.68	0.58		63	Fe(III) A
	0.32	0.51	0.33		24	Fe(III) B	0.32	0.51	0.33		24	Fe(III) B
	1.13	2.62	0.29		13	Fe(II) C	1.13	2.62	0.29		13	Fe(II) C
300	0.36	0.87	0.63		63	Fe(III) A						
	0.36	0.47	0.35		27	Fe(III) B						
	1.13	2.65	0.35		10	Fe(II) C						
350							0.38	1.26	0.72		67	Fe(III) A
							0.37	0.73	0.53		26	Fe(III) B
							1.15	2.59	0.39		7	Fe(II) C
400	0.36	1.14	0.66		69	Fe(III) A	0.39	1.29	0.67		67	Fe(III) A
	0.36	0.58	0.40		29	Fe(III) B	0.35	0.76	0.44		28	Fe(III) B
	1.21	2.59	0.20		2	Fe(II) C	1.11	2.65	0.27		5	Fe(II) C
450	0.37	1.37	0.66		63		0.44	1.29	0.65		49	Fe(III) A
	0.37	0.82	0.48		37	Fe(III) A	0.42	0.82	0.38		12	Fe(III) B
						Fe(III) B	1.01	2.44	0.63		39	Fe(II) C
500	0.37	1.43	0.64		60	Fe(III) A	0.45	1.29	0.68		45	Fe(III) A
	0.37	0.85	0.50		40	Fe(III) B	0.42	0.82	0.43		15	Fe(III) B
							1.06	2.42	0.60		40	Fe(II) C
550	0.37	1.45	0.57		56	Fe(III) A	0.43	1.31	0.64		44	Fe(III) A
	0.36	0.87	0.50		44	Fe(III) B	0.41	0.81	0.43		15	Fe(III) B
							1.06	2.34	0.62		41	Fe(II) C
600	0.35	1.50	0.57		56	Fe(III) A	0.44	1.47	0.73		44	Fe(III) A
	0.39	1.00	0.66		44	Fe(III) B	0.47	1.01	0.36		17	Fe(III) B
							1.13	2.20	0.63		39	Fe(II) C
650	0.35	1.55	0.65		56	Fe(III) A						
	0.37	0.99	0.51		44	Fe(III) B						
700	0.35	1.56	0.66		53	Fe(III) A	0.39	1.54	0.70		40	Fe(III) A
	0.36	0.96	0.51		47	Fe(III) B	0.42	0.88	0.50		21	Fe(III) B
							1.25	2.21	0.77		39	Fe(II) C
750	0.36	1.44	0.85		51	Fe(III) A						
	0.35	0.86	0.49		31	Fe(III) B						
	0.36	−0.24	0.50	50.0	18	α-Fe_2O_3						
800	0.39	1.42	0.75		54	Fe(III) A	0.36	1.03	0.89		46	Fe(III) A
	0.37	0.83	0.46		32	Fe(III) B	0.92	1.49	0.53		10	Fe(II) D
	0.36	−0.22	0.48	50.0	14	α-Fe_2O_3	1.10	2.28	0.72		44	Fe(II) E
850	0.34	1.39	0.75		51	Fe(III) A	0.34	0.77	0.21		5	Fe(III) A
	0.33	0.80	0.46		29	Fe(III) B	1.19	2.29	0.53		54	Fe(II) D
	0.33	−0.26	0.48	50.4	20	α-Fe_2O_3	0.90	1.18	0.60		23	Fe(II) E
							0.87	2.22	0.38		19	Fe(II) F
900	0.30	1.07	0.74		45	Fe(III) A	0.36	0.77	0.34		13	Fe(III) A
	0.32	0.63	0.32		14	Fe(III) B	1.20	2.27	0.51		48	Fe(II) D
	0.35	−0.23	0.62	49.3	41	α-Fe_2O_3	0.92	1.07	0.43		17	Fe(II) E
							0.87	2.12	0.42		22	Fe(II) F
950	0.31	0.93	0.54		44	Fe(III) A						
	0.33	0.57	0.25		10	Fe(III) B						
	0.37	−0.23	0.44	50.0	46	α-Fe_2O_3						
1000	0.27	0.90	0.46		39	Fe(III) A						
	0.30	0.51	0.20		9	Fe(III) B						
	0.36	−0.22	0.41	50.2	53	α-Fe_2O_3						
1050	0.30	0.74	0.51		39	Fe(III) A	0.27	0.71	0.34		10	Fe(III) G
	0.36	−0.22	0.41	50.2	61	α-Fe_2O_3	1.09	2.38	0.45		40	Fe(II) D
							0.89	1.22	0.56		25	Fe(II) E
							0.98	1.91	0.49		15	Fe(II) F
							0.00	0.00	0.27	33.0	10	Fe(0)

(continued on next page)

Table 1 (*continued*)

T (°C)	Margins						Cores					
	δ (mm/s)	ΔE_Q or $2\varepsilon_Q$ (mm/s)	Γ (mm/s)	H (T)	A (%)	Attrib.	δ (mm/s)	ΔE_Q or $2\varepsilon_Q$ (mm/s)	Γ (mm/s)	H (T)	A (%)	Attrib.
1100	0.30	0.79	0.51		33	Fe(III) A	0.24	0.49	0.34		8	Fe(III) G
	0.37	−0.22	0.46	49.9	67	α-Fe_2O_3	1.12	2.42	0.39		25	Fe(II) D
							0.86	1.59	0.54		24	Fe(II) E
							1.08	1.81	0.44		22	Fe(II) F
							0.00	−0.01	0.31	33.0	21	Fe(0)

δ: isomer shift; ΔE_Q: quadrupole splitting for non-magnetic or $2\varepsilon_Q$: quadrupole shift for magnetic sub-spectra; Γ: full linewidth at half maximum; H: internal magnetic field; A: fractional area. δ values are related to metallic α-Fe at RT. Sites A, B and C are attributed to mineral phases originally present in starting clayey material and broken down (or partially so) during firing. Sites D, E F, G and H are due to newly crystallised mineral phases. Al-Hem: Al-substituted hematite; Fe(0): metallic α-Fe_2O_3/Fe. Sites A and B refer to octahedral Fe(III), site C to octahedral Fe(II), sites D, E and F to spinel, and sites G to tetrahedral Fe(III).

mm/s), δ of 0.32 mm/s and Γ of 0.58 mm/s. They represent 63% and 24% of the total area, respectively. An additional octahedral site (site C, ΔE_Q=2.62 mm/s, δ=1.11 mm/s, Γ=0.30 mm/s, 13% of the total area) is due to Fe(II) (Fig. 3, Table 1). Although several Fe-bearing phases are present in the clay, comparisons with data from De Grave et al. (1987) and Stevens et al. (1998) indicate that Fe(II) is basically related to chlorite, whereas the Fe(III) signal is congruent with chlorite and illite sites (Stevens et al., 1998). Moreover, no superparamagnetic phenomena were revealed at low temperature (80 K measurement), indicating that Fe oxides or oxyhydroxides are absent, at least as particles with grain size greater than 5 nm (Murad and Johnston, 1987).

The 32 disks prepared with clayey material AES7a were fired in both reducing and oxidising conditions, in the thermal range 300–1100 °C, according to the procedure described in Section 2. Macroscopically, the ceramic products differ greatly in colour and internal structure, depending on redox conditions and firing temperature. In particular, in *pit firing* conditions, uniformly dark grey (lower temperatures) to very dark grey (higher temperatures) ceramic products were obtained, whereas in *kiln firing* conditions, the products displayed a sandwich structure, characterised by a dark grey core and a brown to red margin, depending on firing temperature, similar to that observed in ancient pottery (Nodari et al., 2004; Maritan et al., 2005).

The mineral assemblages of the different runs were determined by XRD and are shown in the bar diagrams of Figs. 4 and 5 for *pit* and *kiln firing* conditions, respectively.

In *pit firing* conditions, a series of reactions were detected with increasing temperature (Fig. 4). Chlorite began to decompose between 500 °C, with the disappearance of the (002) reflection, and 650 °C, when the (001) reflection also disappeared. Illite decomposed

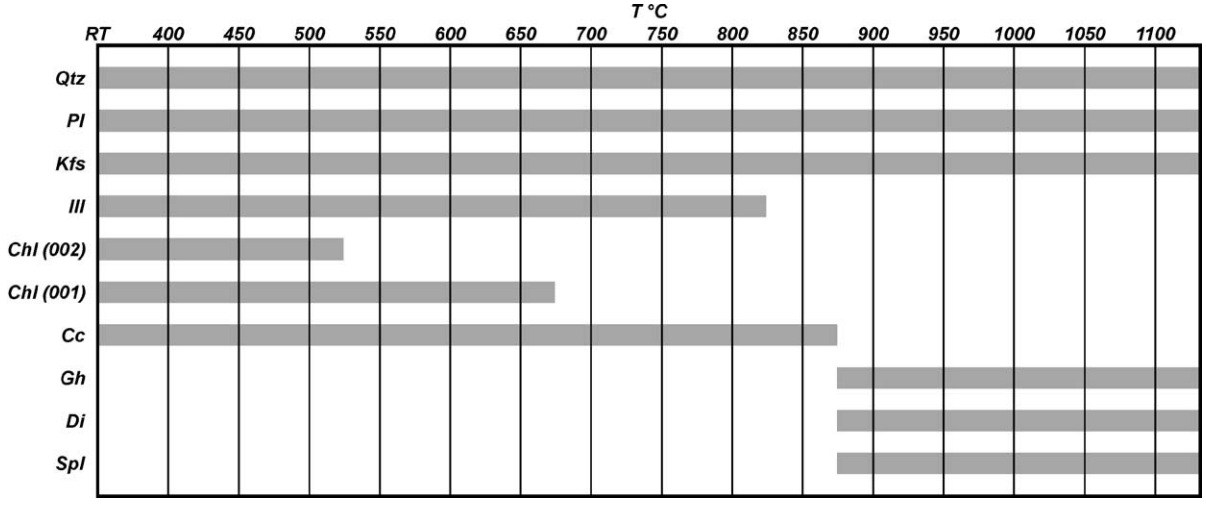

Fig. 4. Bar diagram showing variations in mineral assemblages with increasing temperature during experiments in *pit firing* conditions. Qtz: quartz; Pl: plagioclase; Kfs: K-feldspar; Ill: illite; Chl: chlorite; Cc: calcite; Gh: gehlenite; Di: diopside; Spl: spinel. RT: room temperature.

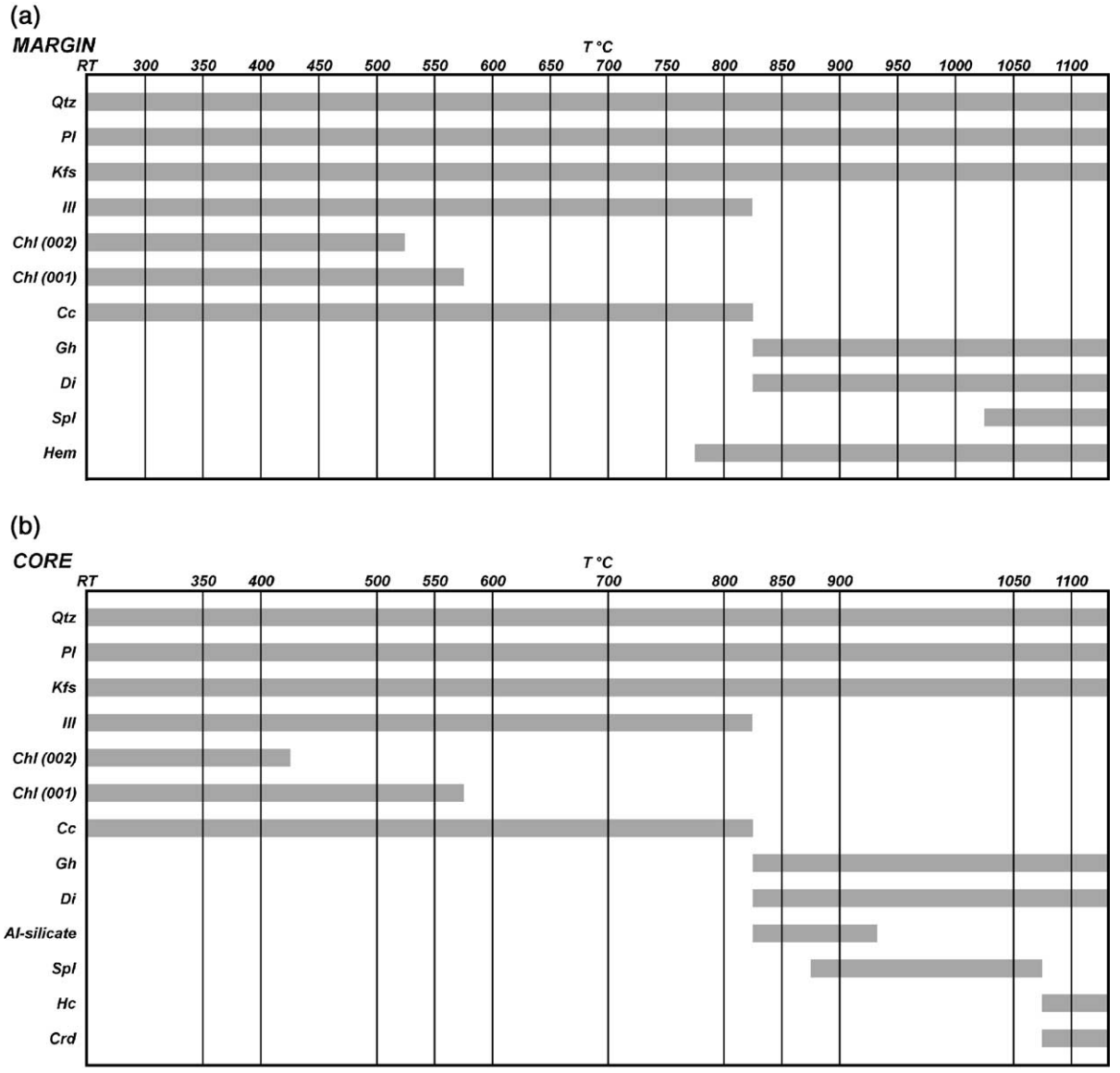

Fig. 5. Bar diagrams showing variations in mineral assemblages in the margin (a) and in the core (b) of samples prepared in *kiln firing* conditions. Al-silicate: Al-silicate of Mg; Hem: hematite; Hc: hercynite; Crd: cordierite. Other abbreviations as in Fig. 4.

at 800 °C, a much lower temperature than reported elsewhere in the literature (Duminuco et al., 1996; Riccardi et al., 1999). Further increases in temperature caused the decarbonation of calcite and the crystallisation of gehlenite, diopside and spinel between 850 and 900 °C.

Also in the case of *kiln firing* experiments, chlorite was the first mineral phase to decompose (Fig. 5) between 400–500 °C (in the core) and 500–550 °C (in the margin). Calcite and illite devolatilisation was observed between 800 and 850 °C, and was associated with the formation of gehlenite and diopside. At further temperature increments, the mineral assemblage in the margin began to differentiate from that in the core, with the formation of hematite in the margin at 800 °C and spinel at 1050 °C, indicating that oxidising firing conditions affect reactions in this portion of the ceramic body. Contrasting mineral assemblages were observed in the core, where an Mg–Al-silicate and spinel form at the expense of chlorite and illite (Holdaway and Lee,

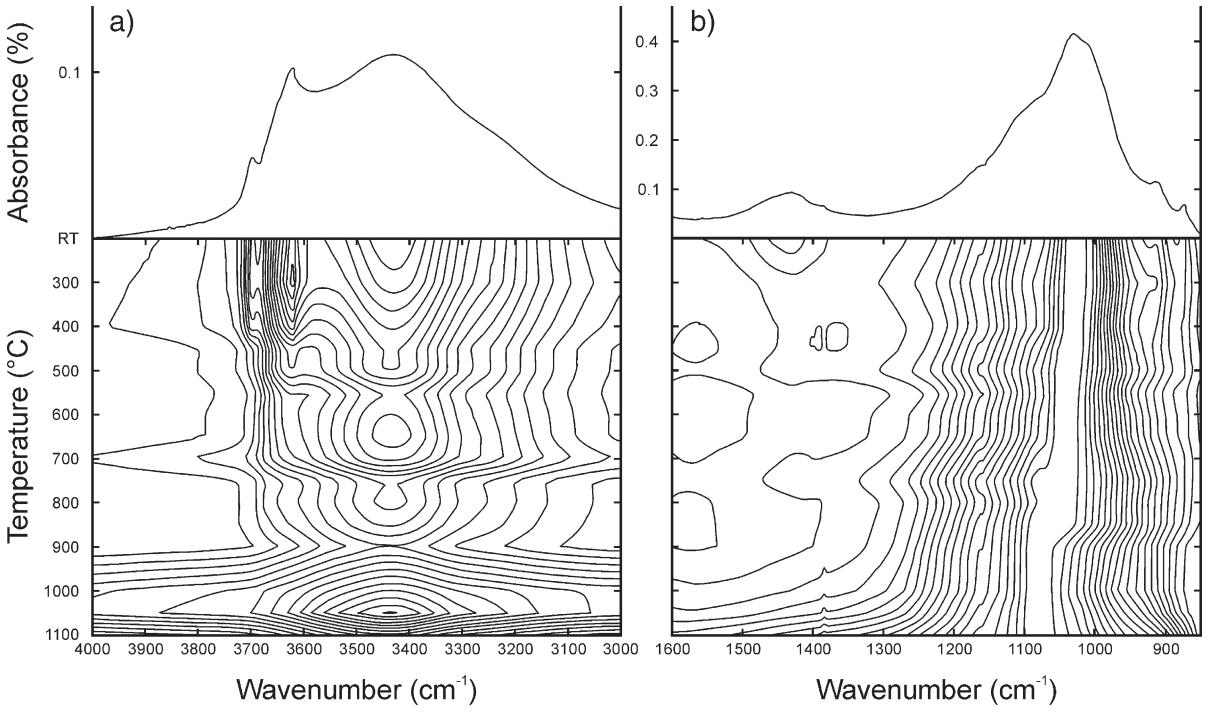

Fig. 6. Evolution of FTIR spectra with temperature at margin of samples prepared in *kiln firing* conditions. (a) OH stretching region; (b) Si–O stretching region. Contour curves refer to Absorbance.

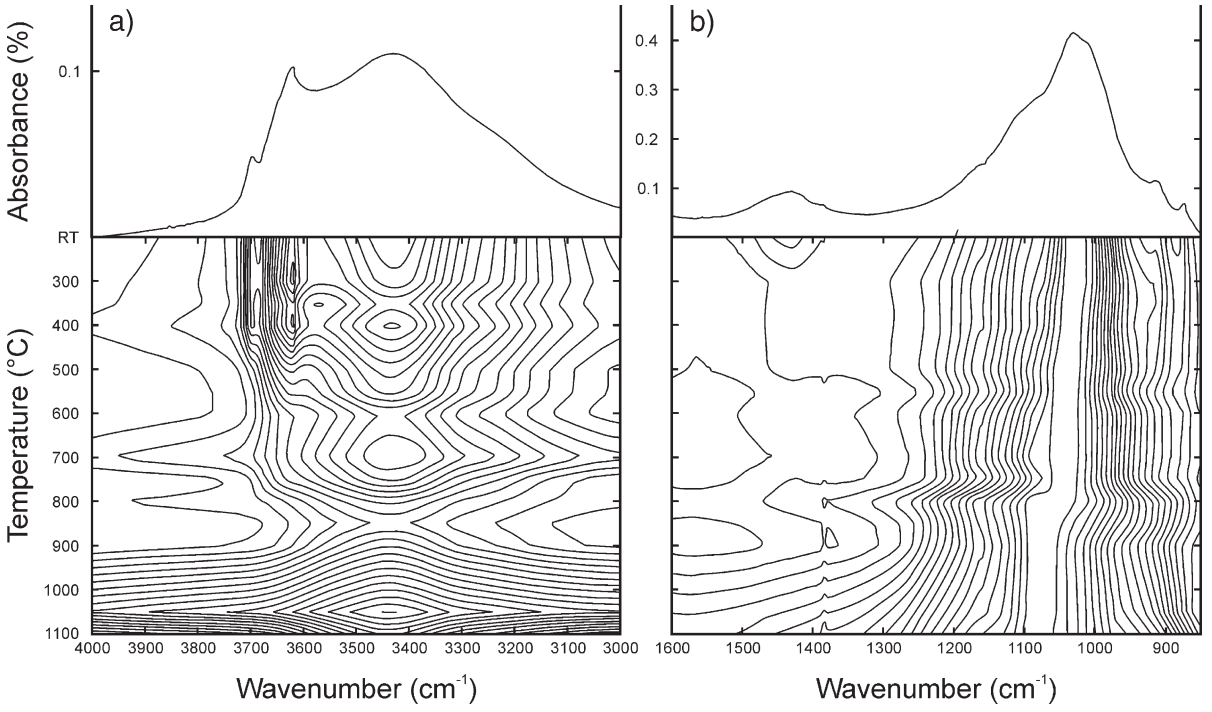

Fig. 7. Evolution of FTIR spectra with temperature at core of samples prepared in *kiln firing* conditions. (a) OH stretching region; (b) Si–O stretching region. Contour curves refer to Absorbance.

Table 2
80 K Mössbauer parameters for some significant samples prepared in *kiln firing* conditions

T (°C)	Margins						Cores					
	δ (mm/s)	ΔE_Q or $2\varepsilon_Q$ (mm/s)	Γ (mm/s)	H (T)	A (%)	Attrib.	δ (mm/s)	ΔE_Q or $2\varepsilon_Q$ (mm/s)	Γ (mm/s)	H (T)	A (%)	Attrib.
Clay	0.48	0.77	0.57		63	Fe(III) A	0.48	0.77	0.57		63	Fe(III) A
	0.46	0.66	0.39		23	Fe(III) B	0.46	0.66	0.39		23	Fe(III) B
	1.24	2.87	0.36		14	Fe(II) C	1.24	2.87	0.36		14	Fe(II) C
550							0.49	1.41	0.62		40	Fe(III) A
							0.45	0.81	0.43		14	Fe(III) B
							1.18	2.43	0.71		46	Fe(II) C
700	0.44	1.62	0.87		51	Fe(III) A	0.56	1.57	0.87		44	Fe(III) A
	0.53	1.07	0.57		49	Fe(III) B	0.44	1.02	0.48		23	Fe(III) B
							1.25	2.35	0.68		33	Fe(II) C
850							0.34	0.86	0.34		7	Fe(III) B
							1.35	2.51	0.49		52	Fe(II) D
							1.06	1.31	0.36		21	Fe(II) E
							1.00	2.51	0.47		20	Fe(II) F
1050	0.39	0.77	0.53		36	Fe(III) A						
	0.49	−0.21	0.42	52.9	64	Fe(III) B						
1100							0.35	0.49	0.43		7	Fe(III) G
							1.14	2.89	0.44		25	Fe(II) D
							1.07	1.96	0.52		27	Fe(II) E
							1.23	2.38	0.34		22	Fe(II) F
							0.11	0.02	0.28	33.7	19	Fe(0)

Abbreviations and site attributions as in Table 1.

1977; Jordan et al., 1999) between 850 and 900 °C. In an Al-rich system (Heimann, 1989), they are precursors of cordierite and hercynite, which were actually detected at 1100 °C. The occurrence of cordierite indicates reducing conditions in the core, with $f(O_2)$ lower than 10^{-4} bar (Heimann et al., 1980).

In addition, in both *pit* and *kiln firing*, the intensity of plagioclase and K-feldspar peaks in XRD patterns rises with temperature, indicating that continuous reactions such as: (i) 0.4 illite + 1.2 calcite → 0.4 K-feldspar + 0.6 gehlenite + quartz + 1.6 H_2O + 1.2 CO_2 and (ii) gehlenite + quartz → diopside + anorthite, also occur during firing (Peters and Iberg, 1978; Dondi et al., 1995; Duminuco et al., 1996, 1998).

The progressive dehydroxylation and distortion of the silicate structure with temperature were also monitored by FTIR spectroscopy.

The main variations observed in the FTIR patterns with increasing temperature in both margin (Fig. 6) and core (Fig. 7) of *kiln-fired* specimens were due to the

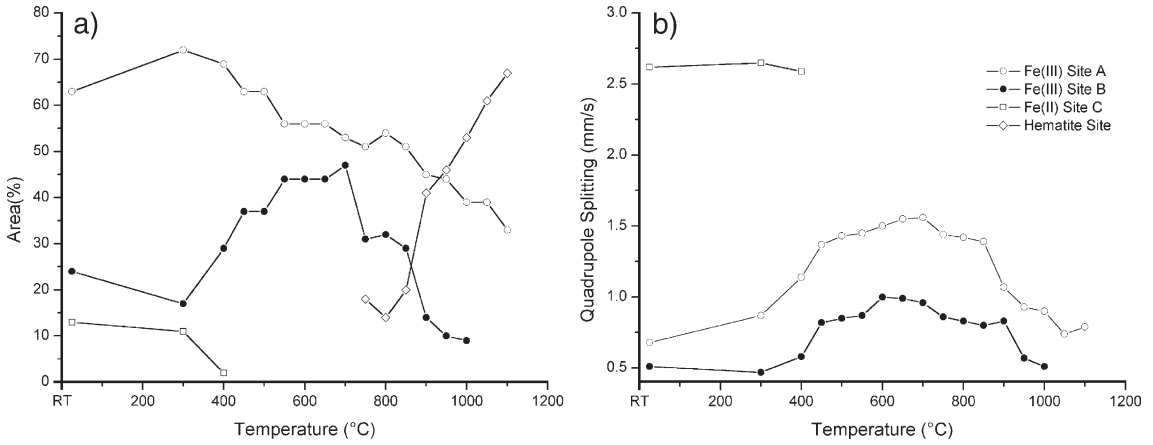

Fig. 8. Site area (a) and quadrupole splitting (ΔE_Q) parameter (b) vs. firing temperature in margin of samples prepared in *kiln firing* conditions. Sites A, B and C are also observed in starting clayey material (RT); Al-substituted hematite sites appear after firing.

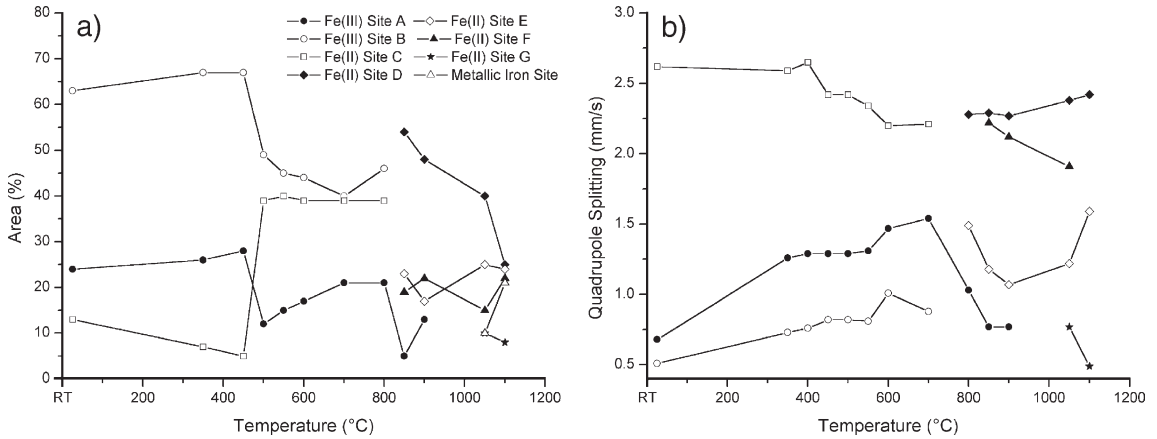

Fig. 9. Site area (a) and quadrupole splitting (ΔE_Q) (b) vs. firing temperature, in core of samples prepared in *kiln firing* conditions. Sites A, B and C are also observed in starting clayey material (RT); sites D, E, F, G and metallic Fe site are produced by firing.

weakening of the hydroxyl stretching bands at 3696 and 3621 cm^{-1}, which progressively lost definition until complete disappearance at 450 °C. Phyllosilicates also started to decompose at 500 °C, causing progressive broadening of the Si–O band until vitrification occurred at 1000 °C.

An additional modification, observed exclusively in the margin, was oxidation of Fe(II) in silicates, as shown by the progressive reduction of the relative area of site C in Mössbauer spectra (Tables 1 and 2), until complete oxidation was achieved between 400 and 450 °C (Fig. 8a). Consequently, Fe(III) in site B increased, while the relative area of site A decreased (Fig. 8a). Between 700 and 750 °C, the percentage of both sites A and B rapidly decreased with the appearance of a new oxidic phase. The hyperfine parameters of the narrow sextet in the RT Mössbauer spectra are consistent with those of an Al-substitute hematite (Murad and Johnston, 1987), the increasing of the relative area indicating the progressive increase of its concentration. These transformations also affected the ΔE_Q values of sites A and B: these values increased with

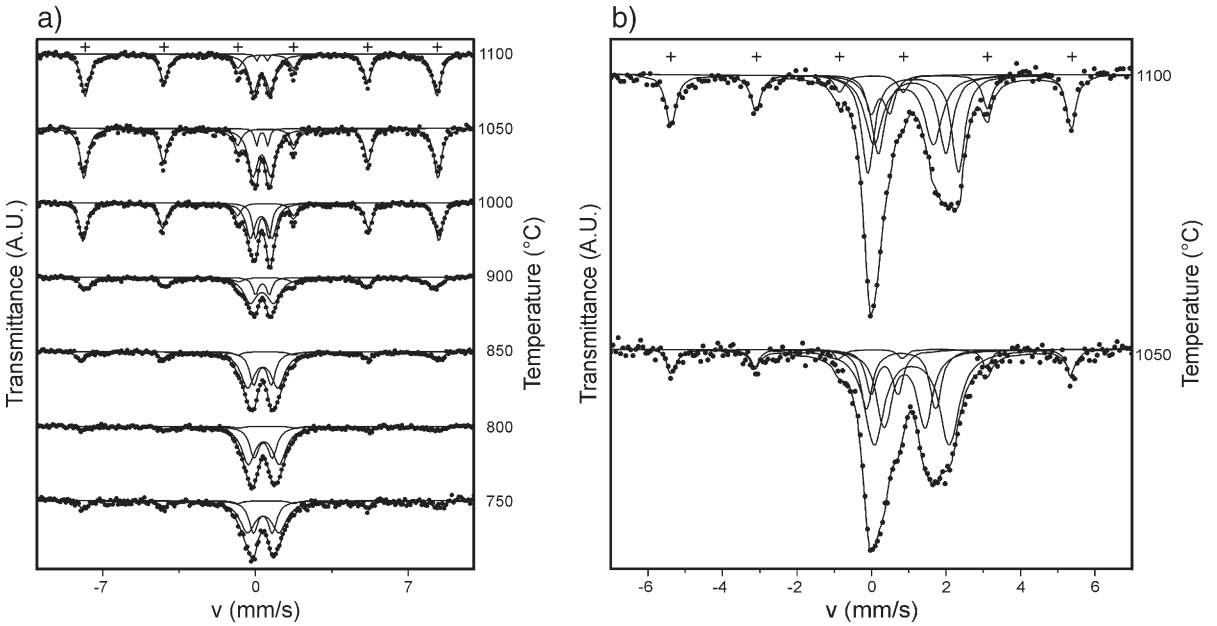

Fig. 10. Mössbauer spectra of samples prepared in *kiln firing* conditions. (a) Spectra obtained from margin in the range 750–1100 °C, in order to emphasize formation of hematite; crosses mark hematite sextet. (b) Spectra obtained from core in the range 1050–1100 °C, in order to emphasize formation of metallic Fe; crosses mark Fe(0) sextet. A.U. = arbitrary unit.

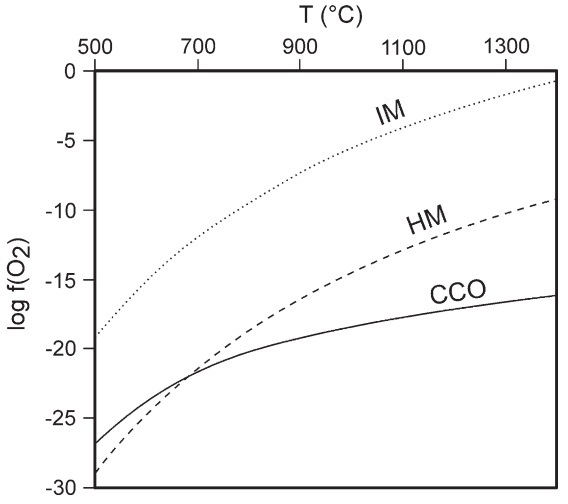

Fig. 11. Plot of log $f(O_2)$ vs. firing temperature for hematite–magnetite (HM), metallic iron–magnetite (IM) and carbon–carbon oxide (CCO) oxygen fugacity buffers, calculated with Vertex software package (Connolly, 1990), using thermodynamic database of Holland and Powell (1998) and hybrid equation of state for GCOH fluids of Connolly and Cesare (1993).

dehydroxylation of phyllosilicates from 300 to 450 °C, remained nearly constant between 450 and 850 °C, and decreased above 850 °C, indicating that Fe (III) is re-allocated in new and more stable structural sites of hematite, gehlenite and diopside (Fig. 8b). The large values of ΔE_Q for site A and the broad linewidth were probably due to the presence of slightly different sites, with differing chemical surroundings and/or site distortions, as is typical for structural Fe in silicates.

A different situation was observed in the core of ceramics produced in *kiln firing* conditions. Mössbauer spectra show progressive Fe reduction and breakdown of silicates with increasing temperature (Figs. 9 and 10). At 850 °C, a Fe(II) spinel was detected (sites D, E and F in Fig. 9a) and Fe was completely reduced at 900 °C. Moreover, at 1000 °C, metallic Fe formed, due to further reduction of structural Fe(II) in silicates, whereas that in spinel apparently remained unaffected. Above 1000 °C, part of the structural Fe(II) oxidised to tetrahedral Fe(III) (site G in Fig. 9a). Hyperfine parameters for Fe(II) in site C basically remained constant throughout the firing process. The ΔE_Q of the various sites changed congruently (Fig. 9b).

In addition, 5700, 1629 and 963 ppm of carbon, probably as graphite, were measured by EA in the core of samples fired at 900, 1050 and 1100 °C, respectively. Therefore, graphite buffered $f(O_2)$ in the core up to 1100 °C, although oxidation progressively reduced its total amount. Congruently, EA measurements on sample

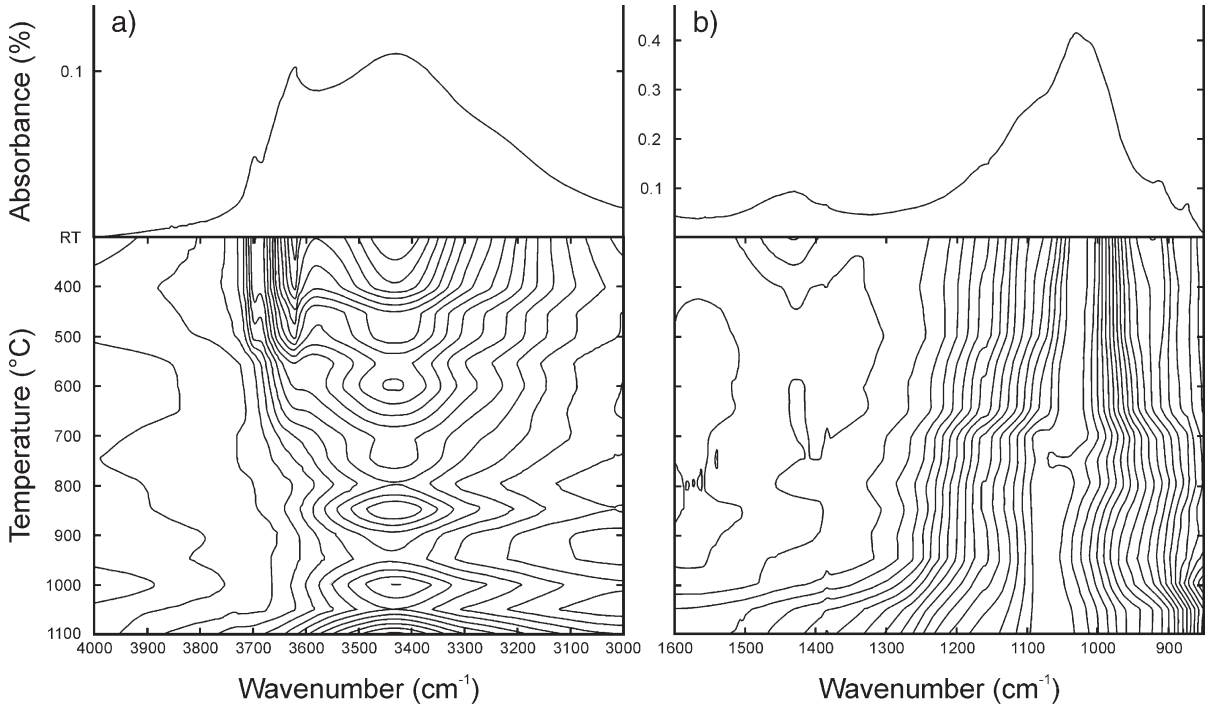

Fig. 12. Evolution of FTIR spectra with temperature in samples prepared in *pit firing* conditions. (a) OH stretching region; (b) Si–O stretching region. Contour curves refer to Absorbance.

Table 3
Room temperature Mössbauer parameters for samples prepared in *pit firing* conditions

T (°C)	δ (mm/s)	ΔE_Q or $2\varepsilon_Q$ (mm/s)	Γ (mm/s)	H (T)	A (%)	Attributions
Clay	0.35	0.68	0.58		63	Fe(III) A
	0.32	0.51	0.33		24	Fe(III) B
	1.13	2.62	0.29		13	Fe(II) C
400	0.44	1.04	0.62		42	Fe(III) A
	0.37	0.59	0.41		26	Fe(III) B
	1.12	2.61	0.44		32	Fe(II) C
450	0.42	1.09	0.60		28	Fe(III) A
	0.32	0.60	0.42		17	Fe(III) B
	1.13	2.65	0.45		21	Fe(II) C
	1.13	2.26	0.52		33	Fe(II) D
500	0.42	1.09	0.60		30	Fe(III) A
	0.32	0.60	0.42		14	Fe(III) B
	1.13	2.71	0.37		24	Fe(II) C
	1.12	2.25	0.53		32	Fe(II) D
550	0.43	1.23	0.60		35	Fe(III) A
	0.38	0.62	0.32		6	Fe(III) B
	1.10	2.60	0.38		30	Fe(II) C
	1.05	2.15	0.50		28	Fe(II) D
600	0.42	1.21	0.67		38	Fe(III) A
	0.42	0.61	0.33		5	Fe(III) B
	1.11	2.51	0.41		30	Fe(II) C
	1.05	2.06	0.52		27	Fe(II) D
650	0.44	1.05	0.70		37	Fe(III) A
	1.09	2.53	0.43		33	Fe(II) C
	1.04	2.02	0.50		30	Fe(II) D
700	0.42	1.00	0.74		12	Fe(III) A
	1.13	2.52	0.47		34	Fe(II) C
	1.06	2.05	0.49		30	Fe(II) D
	1.00	1.48	0.55		24	Fe(II) E
750	1.12	2.53	0.48		34	Fe(II) C
	1.07	2.03	0.39		24	Fe(II) D
	1.01	1.60	0.71		42	Fe(II) E
800	1.12	2.51	0.47		38	Fe(II) C
	1.07	2.02	0.37		22	Fe(II) D
	1.02	1.57	0.68		40	Fe(II) E
850	1.14	2.46	0.45		38	Fe(II) C
	1.09	1.98	0.33		19	Fe(II) D
	0.99	1.50	0.71		43	Fe(II) E
900	1.11	2.46	0.42		34	Fe(II) C
	1.05	1.92	0.37		27	Fe(II) D
	0.94	1.19	0.67		39	Fe(II) E
950	1.12	2.21	0.51		35	Fe(II) C
	0.87	1.96	0.40		24	Fe(II) D
	0.88	1.18	0.57		36	Fe(II) E
	−0.10	0.12	0.30	33.0	4	Fe(0)
1000	1.13	2.08	0.53		35	Fe(II) C
	0.86	1.89	0.41		26	Fe(II) D
	0.90	1.07	0.54		31	Fe(II) E
	−0.03	0.06	0.30	33.2	8	Fe(0)
1050	1.10	2.08	0.53		30	Fe(II) C
	0.83	1.88	0.44		27	Fe(II) D
	0.85	1.10	0.59		30	Fe(II) E
	−0.04	0.05	0.49	32.7	12	Fe(0)
1100	1.18	2.09	0.46		31	Fe(II) C
	0.86	1.86	0.44		29	Fe(II) D
	0.85	1.32	0.85		29	Fe(II) E
	−0.01	0.05	0.38	33.0	12	Fe(0)

Abbreviations and site attributions as in Table 1.

fired at 1100 °C in reducing conditions provided higher C content (2336 ppm).

The presence of graphite in the core and that of hematite in the margin at 1100 °C indicates that $f(O_2)$ is buffered to $1.93 \cdot 10^{-18}$ bar in the core and higher than $9.96 \cdot 10^{-5}$ bar in the margin (Fig. 11). In the simplest case, Fick's laws relate the flux of component i (J_i), the concentration gradient of component i (dC_i/dx) and the change in concentration of component i with time (dC_i/dt) by a single thermodynamic diffusion coefficient (D_i):

$$J_i = -D_i \cdot dC_i/dx; \quad (1)$$

$$dC_i/dt = D_i \cdot \partial^2 C_i/\partial x^2. \quad (2)$$

Considering a thickness of 1.5 cm, and therefore a half-distance of 0.75 cm from core to margin, and a residence time of 6 h, a minimum gradient of $1.33 \cdot 10^{-4}$ bar/cm and a maximum diffusion coefficient of $2.6 \cdot 10^{-5}$ cm^2/s can be calculated for oxygen.

As regards ceramics produced in *pit firing* conditions, changes in FTIR spectra with increasing temperature were relatively similar to those observed in *kiln firing*

Table 4
80 K Mössbauer parameters for some significant samples prepared in *pit firing* conditions

T (°C)	δ (mm/s)	ΔE_Q or $2\varepsilon_Q$ (mm/s)	Γ (mm/s)	H (T)	A (%)	Attributions
Clay	0.48	0.77	0.57		63	Fe(III) A
	0.46	0.66	0.39		23	Fe(III) B
	1.24	2.87	0.36		14	Fe(II) C
550	0.52	1.25	0.58		28	Fe(III) A
	0.45	0.82	0.51		14	Fe(III) B
	1.22	2.87	0.46		34	Fe(II) C
	1.23	2.29	0.47		24	Fe(II) D
650	0.57	1.12	0.72		30	Fe(III) A
	1.16	2.91	0.48		17	Fe(II) C
	1.18	2.31	0.72		54	Fe(II) D
1000	1.30	2.71	0.49		31	Fe(II) C
	1.04	2.86	0.36		28	Fe(II) D
	1.14	1.76	0.70		34	Fe(II) E
	0.09	0.09	0.53	34.3	7	Fe(0)

Abbreviations and site attributions as in Table 1.

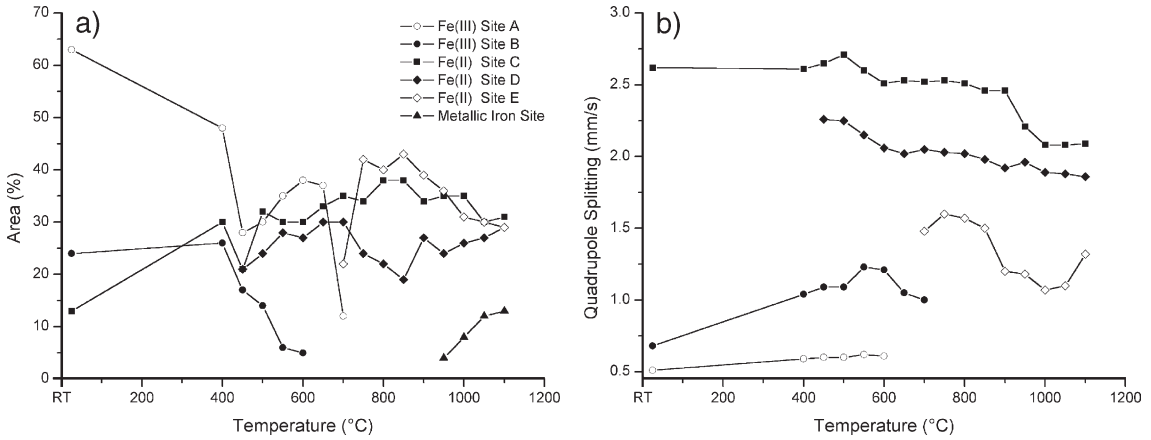

Fig. 13. Site area (a) and quadrupole splitting (b) vs. firing temperature samples prepared in *pit firing* conditions. Sites A, B and C are also observed in starting clayey material (RT); sites D, E and metallic Fe site are produced by firing.

(Fig. 12). Mössbauer data (Tables 3 and 4) show that Fe(III) diminished progressively until complete reduction at 750 °C (Fig. 13a). At 600 and 650 °C, respectively, two new Fe(II) sites appeared (sites D and E in Fig. 13a and b), probably due to chlorite decomposition. At 950 °C, a hyperfine signal due to metallic Fe appeared and its relative area progressively increased, with further temperature increments (Fig. 13). The two different octahedral Fe(III) sites were progressively distorted, as shown by the increase in ΔE_Q values (Fig. 13b). The progressive decay of silicates made increasing amounts of Fe(III) available to reduction and crystallisation of new mineral species, until only one site of Fe(III) was detected at 750 °C, with ΔE_Q parameters intermediate between those observed for Fe(III) sites at 650 °C, indicating that they collapsed into a new intermediate site. The appearance of a tetrahedral site at 700 °C indicated the formation of spinel.

4. Conclusions

Firing temperature in pottery is often estimated on the basis of the absence or occurrence of specific mineral assemblages for a given bulk chemical composition, assuming equilibrium conditions for reactions during firing, as required by thermodynamic calculations and construction of petrogenetic grids. Instead, the set of experiments described in the present paper on clay rich in organic matter shows that redox conditions, heating rate, and residence time all control the temperature of decomposition and crystallisation reactions considerably, indicating that reaction kinetics and the diffusion of gaseous compounds are low on the time scale of the firing process.

In particular, experimental observations allow us to draw the following conclusions:

1) Uniformly dark to very dark grey ceramics were obtained in *pit firing* conditions (i.e., reducing atmosphere, high heating rate, short residence time), due to the presence of organic matter, at least up to 700 °C, crystallisation of spinel at 700 °C, the formation of metallic Fe at 950 °C, and the fact that graphite remains up to the maximum firing temperature. A reducing environment progressively changed Fe(III) to Fe(II) as soon as Fe(III)-bearing mineral phases decomposed.
2) Experiments in *kiln firing* conditions (i.e. oxidising atmosphere, low heating rate, long residence time) invariably produced a sandwich structure, characterised by specimens with a black reduced core and a reddish oxidised margin. The mineral assemblages of core and margin were the same up to 800 °C, indicating that organic matter dominated the different colour of the two parts, persisting in the core and being soon burnt in the margin. The different redox conditions were also marked by the presence of hematite in the margin above 800 °C, and that of spinel and hercynite above 850 °C and of metallic Fe above 1050 °C in the core. Congruently with the presence of metallic Fe, graphite was also detected in the core up to the maximum firing temperature. These differences indicate that, although residence time was longer in *kiln firing* conditions, oxygen diffusion was not sufficiently high to homogenise redox conditions throughout the ceramic paste during firing.

3) Devolatilisation of chlorite and calcite takes place at the same temperature in the core and margin of samples prepared in *kiln firing* conditions; the same reactions occurred at temperatures 50 °C higher when samples were prepared in *pit firing* conditions. Similar differences were recorded for diopside and gehlenite crystallisation, as well as for that of spinel and metallic Fe. This indicates that the differing redox conditions at the core with respect to those at the margin do not significantly influence reaction kinetics. Instead, residence time is the main controlling factor on the temperature for a given reaction, being higher for shorter residence times, and thus indicating that a higher degree of reaction overstepping is required.
4) Illite dehydration in both *pit* and *kiln firing* conditions occurred at lower temperatures than observed elsewhere (Duminuco et al., 1996; Riccardi et al., 1999). One interpretation of this evidence may be the poor diffusion of the gaseous phase through the ceramic body, and therefore the progressive increase in $f(CO_2)$ during burning of organic matter. This might lead to a decrease in the $f(H_2O)$ in the gaseous phase, favouring breakdown reactions of hydroxyl-bearing phases.

Acknowledgements

The Department of Geology, University of Glasgow (Scotland), is acknowledged for granting access to the kiln used for firing experiments in reducing conditions. The authors also thank G. Walton, who revised the English text, *and two anonymous referees for the useful suggestions*. This work was carried out with the financial support of MIUR project "Development and application of mineralogical and petrographical investigation methodologies to the study of archaeological materials".

References

Claret, F., Schafer, T., Bauer, A., Buckau, G., 2003. Generation of humic and fulvic acid from Callovo–Oxfordian clay under high alkaline conditions. The Science of the Total Environment 317, 189–200.

CNR-UNI 10014, 1964. Prove sulle terre: determinazione dei limiti di consistenza (o di Atterber) di una terra.

Connolly, J.A.D., 1990. Multivariable phase diagram: an algorithm based on generalized thermodynamics. American Journal of Science 290, 666–718.

Connolly, J., Cesare, B., 1993. C–O–H–S fluid composition and oxygen fugacity in graphitic metapelites. Journal of Metamorphic Geology 11, 379–388.

De Benedetto, G.E., Laviano, R., Sabbatini, L., Zambonin, G.P., 2002. Infrared spectroscopy in the mineralogical characterisation of ancient pottery. Journal of Cultural Heritage 3, 177–186.

De Grave, E., Vandenbruwaene, J., Van Bockstael, M., 1987. ^{57}Fe Mössbauer spectroscopic analysis of chlorite. Physics and Chemistry of Minerals 15, 173–180.

De Nobili, M., Maggioni, A., 1993. Influenza della sostanza organica sulle proprietà fisiche del suolo. In: Nannipieri, P. (Ed.), Ciclo della Sostanza Organica nel Suolo, pp. 43–54.

Dondi, M., Ercolani, G., Guarini, G., Marsigli, M., Venturi, I., 1995. Evoluzione della microstruttura durante la cottura rapida di impasti per piastrelle porose. Ceramurgia 25 (6), 301–314.

Duminuco, P., Riccardi, M.P., Messiga, B., Setti, M., 1996. Modificazioni tessiturali e mineralogiche come indicatori della dinamica del processo di cottura di manufatti ceramici. Ceramurgia 26 (5), 281–288.

Duminuco, P., Messiga, B., Riccardi, M.P., 1998. Firing process of natural clays: some microtextures and related phase compositions. Thermochimica Acta 321, 185–190.

Farmer, V.C., 1974. Infrared Spectra of Minerals, Ed. Mineralogical Society, London.

Gosselain, O.P., 1992. Bonfire of the enquiries: pottery firing temperatures in archaeology: what for? Journal of Archaeological Science 19, 243–259.

Heimann, R.B., 1989. Assessing the technology of ancient pottery: the use of ceramic phase diagrams. Archeomaterials 3, 123–148.

Heimann, R.B., Maggetti, M., Einfalt, H., 1980. Zum Verhalten des Eisens beim Brennen eines kalkhaltigen illitischen Tons unter reduzierenden Bedingungen. Berichte der Deutschen Keramischen Gesellschaft 57, 145–152.

Holdaway, M.J., Lee, S.M., 1977. Fe–Mg cordierite stability in high-grade pelitic rocks based on experimental, theoretical and natural observations. Contributions to Mineralogy and Petrology 63, 175–198.

Holland, T.J.B., Powell, R., 1998. An internally consistent thermodynamic data set for phases of petrological interest. Journal of Metamorphic Geology 16, 309–344.

Husein Malkawi, A.I., Alawneh, A.S., Abu-Safaqah, O.T., 1999. Effect of organic matter on the physical and physicochemical proprieties of an illitic soil. Applied Clay Science 14, 257–278.

Johnson, J.S., Clark, J., Miller-Antonio, S., Robins, D., Schiffer, M.B., Skibo, J.M., 1988. Effect of firing temperature on the fate of naturally occurring organic matter in clay. Journal of Archaeological Science 15, 403–414.

Jordan, M.M., Boix, A., Sanfeliu, T., De La Fuente, C., 1999. Firing transformations of Cretaceous clays used in the manufacturing of ceramic tiles. Applied Clay Science 14, 225–234.

Krajewski, A., Fabbri, B., Fiori, C., Valmori, R., 1985. Analisi mineralogiche di materie prime ceramiche con computer. Ceramica Informazione 232, 391–396.

Mackenzie, R.C., 1957. The Differential Thermal Investigation of Clay. Mineralogical Society, London.

Maritan, L., Mazzoli, C., Nodari, L., Russo, U., 2005. Second Iron Age grey pottery from Este (north-eastern Italy): study of provenance and technology. Applied Clay Science 29, 31–44.

Marsigli, M., Dondi, M., 1997. Plasticità delle argille italiane per i laterizi e previsione del loro comportamento in foggiatura. L'industria dei laterizi 46, 214–222.

Murad, E., Johnston, J.H., 1987. Iron oxides and oxyhydroxides. In: Long, G.J. (Ed.), Mössbauer Spectroscopy Applied to Inorganic Chemistry. Plenum Press, New York, pp. 507–582.

Nannipieri, P., 1993. Ciclo Della Sostanza Organica Nel Suolo. Patron Editore, Bologna.

Nodari, L., Maritan, L., Mazzoli, C., Russo, U., 2004. Sandwich structures in the Etruscan–Padan type pottery. Applied Clay Science 27, 119–128.

Peters, T., Iberg, R., 1978. Mineralogical changes during firing of calcium-rich brick clays. American Ceramic Society Bulletin 57 (5), 503–509.

Ragazzi, E., Roghi, G., Giaretta, A., Gianolla, P., 2003. Classification of amber based on thermal analysis. Thermochimica Acta 404, 43–54.

Riccardi, M.P., Messiga, B., Duminuco, P., 1999. An approach to the dynamics of clay firing. Applied Clay Science 15, 393–409.

Rivero, C., Senesi, N., Paolini, J., D'Orazio, V., 1998. Characteristics of humic acids of some Venezuelan soils. Geoderma 81, 227–239.

Rye, O., 1981. Pottery Technology: Principles and Reconstruction. Taraxacum Inc., Washington.

Stevens, J.G., Khasanov, A.M., Miller, J.W., Pollak, H., Li, Z., 1998. Mössbauer Mineral Handbook. Mössbauer Effect Data Center 307.

Stucki, J.W., Bish, D.L., 1990. Thermal Analysis in Clay Science. Clay Minerals Society.